

# Lab on a Chip

Accepted Manuscript



This is an *Accepted Manuscript*, which has been through the Royal Society of Chemistry peer review process and has been accepted for publication.

*Accepted Manuscripts* are published online shortly after acceptance, before technical editing, formatting and proof reading. Using this free service, authors can make their results available to the community, in citable form, before we publish the edited article. We will replace this *Accepted Manuscript* with the edited and formatted *Advance Article* as soon as it is available.

You can find more information about *Accepted Manuscripts* in the [Information for Authors](#).

Please note that technical editing may introduce minor changes to the text and/or graphics, which may alter content. The journal's standard [Terms & Conditions](#) and the [Ethical guidelines](#) still apply. In no event shall the Royal Society of Chemistry be held responsible for any errors or omissions in this *Accepted Manuscript* or any consequences arising from the use of any information it contains.

# Chemical-Assisted Femtosecond Laser Writing of Lab-in-Fibers

Moez Haque,\* Kenneth K. C. Lee, Stephen Ho, Luís A. Fernandes, and Peter R. Herman

Received Xth XXXXXXXXXXXX 20XX, Accepted Xth XXXXXXXXXXXX 20XX

First published on the web Xth XXXXXXXXXXXX 200X

DOI: 10.1039/b000000x

The lab-on-chip (LOC) platform has presented a powerful opportunity to improve functionalization, parallelization, and miniaturization on planar or multi-level geometries that has not been possible with fiber optic technology. A migration of such LOC devices into the optical fiber platform would therefore open the revolutionary prospect for creating novel lab-in-fiber (LIF) systems on the base of an efficient optical transport highway for multi-functional sensing. For the LIF, the core optical waveguide inherently offers a facile means to interconnect numerous types of sensing elements along the optical fiber, presenting the radical opportunity for optimizing the packaging and densification of diverse components in convenient geometries beyond that available with conventional LOCs. In this paper, three-dimensional patterning inside optical fiber with femtosecond laser writing, together with selective chemical etching, is presented as a powerful tool to form refractive index structures such as optical waveguides and gratings as well as to open buried microfluidic channels and optical resonators inside the flexible and robust glass fiber. In this approach, optically smooth surfaces ( $\sim 12$  nm rms) are introduced for the first time inside the fiber cladding that precisely conform to planar nanograting structures when formed by aberration-free focusing with an oil-immersion lens across the cylindrical fiber wall. This processing has enabled optofluidic components to be precisely embedded within the fiber to be probed by either the single mode fiber core waveguide or laser-formed optical circuits. We establish cladding waveguides, X-couplers, fiber Bragg gratings, microholes, mirrors, optofluidic resonators, and microfluidic reservoirs that define the building blocks for facile interconnection of inline core-waveguide devices with cladding optofluidics. With these components, more advanced, integrated, and multiplexed fiber microsystems are presented demonstrating fluorescence detection, Fabry Perot interferometric refractometry, and simultaneous sensing of refractive index, temperature, and bending strain. The flexible writing technique and multiplexed sensors described here open powerful prospects to migrate the benefits of LOCs into the more flexible and miniature LIF platform for highly functional and distributed sensing capabilities. The waveguide backbone of the LIF inherently provides an efficient exchange of information, combining sensing data that is attractive in telecom networks, smart catheters for medical procedures, compact sensors for security and defense, shape sensors, and low-cost health care products.

## 1 Introduction

Biological and chemical laboratory processes are continuously being advanced by the miniaturization and integration of bulky free-space systems to create more compact and functional lab-on-chip (LOC) devices that typically appear in planar<sup>1</sup> or multilayered<sup>2</sup> geometries. Today, LOCs can interrogate extremely small fluid volumes (pL) with rapid analysis, response, and manipulation times with attractive scaling to massive parallelization capabilities and lowering fabrication costs. This LOC development has recently embraced optofluidic devices that improve the LOC sensing efficacy by combining microfluidic channels with optical sensing elements to harness the novel opportunities of integrated micro- and nano-scale photonics<sup>3–11</sup>. Such integrated optical components may transport laboratory-scale imaging tools and fluorescence-

based detection methods<sup>12</sup> and enable rapid, in-situ optical characterization methods.

Optical fibers have also been exploited towards interrogation and sensing applications. Single mode optical fiber (SMF) is widespread today in guiding encoded light signals over 1.8 billion kilometers of today's telecommunication network with fast data speeds ( $>200,000$  km/s), high modulation rates (100 Gbits/s), and exceptionally low transmission loss (0.2 dB/km). This fiber optic technology can also serve as an efficient optical transport highway for multi-functional sensing when integrated with optical probes and diagnostic devices. Such fiber sensing provides advantages over conventional electronic sensors due to their immunity to electromagnetic interference<sup>13</sup>, compact size, light weight, mechanical flexibility, robustness, chemical inertness, low autofluorescence, biocompatibility, high wettability, and large thermal conductivity that underpin diverse applications for embedded, remote, or distributed sensing in extreme, long distance, or biological environments<sup>14,15</sup>. Hence, the prospect for developing lab-on-fiber (LOF) has recently emerged with

*Department of Electrical and Computer Engineering, Institute for Optical Sciences, University of Toronto, 10 King's College Road, Toronto, Canada. Fax: +1 416 978 3020; Tel: +1 416 978 7039; E-mail: moez.haque@mail.utoronto.ca*

label-free chemical and biological sensing<sup>16,17</sup>, acoustic pressure wave analysis<sup>18</sup>, and trace TNT explosive detection<sup>19</sup>.

One of the challenges in LOF sensing is coupling the core waveguide light to the fiber cladding surface where sensing structures or chemicals can be introduced in a variety of ways such as with electron beam lithography<sup>18</sup>, metallic or dielectric deposition<sup>16,17,20,21</sup>, and thin chemically active coatings<sup>13,19</sup>. A stronger optical probing of analytes has been provided by chemical thinning of standard<sup>22–24</sup> or doped<sup>25,26</sup> fiber cladding to bring a strong probing evanescent field to the cladding surface, but with the disadvantage of creating exceptionally fragile fiber<sup>27</sup>. On the other hand, the glass cladding in typical SMF defines a largely untapped volume constituting more than 99% of the glass fiber cross-sectional area in which LOC components may be considered for their dense integration. With appropriate fabrication tools, the migration of LOC concepts into optical fiber presents the revolutionary prospect to optimize packaging and densification of sensing elements beyond that available for LOF. Hence, three-dimensional (3D) structuring of multiplexed components in lab-in-fiber (LIF) promises to combine sensing data and efficiently exchange information that is attractive in telecom networks, smart 3D shape sensing of catheters, compact sensors for security and defense, and low-cost health care monitors with non-invasive *in vivo* detection that may potentially be distributed over 100s of kilometers on fiber optic highways.

A promising approach to developing LIFs centers on femtosecond lasers that have previously enabled flexible 3D structuring of glass<sup>28–30</sup>. Since the discovery by Davis et al.<sup>31</sup> that strong focusing of femtosecond laser light can induce positive refractive index modification inside bulk fused silica, many types of optical devices<sup>32–43</sup> have been demonstrated as the building blocks for 3D optical circuits as reviewed by Gattass and Mazur<sup>44</sup>. Femtosecond lasers have also been extended into optical fiber to structure fiber Bragg gratings (FBGs) in the core waveguide<sup>17,21,45</sup> and more recently to form 3D optical circuits into the fused silica cladding<sup>46–48</sup> of SMF. The beginning of LIF development is found in attempts to open channels and introduce microfluidics into the fiber core waveguide. “Holey fiber”<sup>49,50</sup> naturally provides strong optical guiding of light when gases or liquids are injected inside the holes, but have been limited in their means to offer distributed or multifunctional sensing. Alternatively, laser machining of microholes<sup>51,52</sup> and optical resonators<sup>53–59</sup> have enabled a basic “top-down” microfluidic building process for LIFs but have generated low-quality surface profiles with significant optical insertion loss. To date, only single-function devices have been introduced inside optical fiber that have been applied towards biological<sup>60,61</sup>, biomedical<sup>62,63</sup>, environmental<sup>14,64</sup>, strain<sup>22,23,25,65</sup>, temperature<sup>52,55,57,58,65–69</sup>, acoustic<sup>16,18</sup>, chemical<sup>16,19,27,70,71</sup>, or pressure<sup>72</sup> sensing. The prospects for overcoming coarse machining surfaces and

multi-component integration have not permitted further advances towards highly functional and multiplexed optofluidic sensing within the promising LIF platform.

Femtosecond laser irradiation followed by chemical etching (FLICE) has emerged as a promising method for 3D writing of microfluidic systems in bulk fused silica glass. FLICE relies on the formation of bulk nanogratings<sup>32,73–78</sup> within laser-modification tracks that are highly susceptible to hydrofluoric acid (HF)<sup>74,75,79</sup> or potassium hydroxide (KOH)<sup>80</sup> etching. Moreover, the combination of FLICE with femtosecond laser waveguide writing has provided a novel means for 3D integration of optical and microfluidic components that underpins new directions in optofluidic microsystems<sup>81–85</sup> as reviewed by Osellame et al.<sup>86</sup> and Xu et al.<sup>87</sup>. Alternatively, Benion and coworkers applied FLICE inside SMF for creating microfluidic networks in fiber cladding to introduce temperature<sup>66</sup> and refractive index<sup>66,88–91</sup> sensing but with large optical insertion losses owing to high roughness on the FLICE-formed surfaces. Recently, FLICE was shown to provide a small 10 nm (rms) surface roughness in bulk fused silica by Ho et al.<sup>92,93</sup> which is motivating the present direction to form 3D optically smooth microfluidic systems within the pure fused silica cladding of fiber and thereby open the novel opportunity for 3D LIF development.

In this paper, we exploit the femtosecond laser to tailor the nanograting formation and refractive index modification previously demonstrated in LOCs and bring the novel 3D LOC functionality into the fused silica platform of SMF. The concept of creating optical circuits within the cladding is further explored as a novel means for 3D integration of optical and microfluidic networks that couple with the fiber core waveguide. This approach is further extended inside a coreless optical fiber as a convenient structure for fusion splicing to SMF. Laser writing by the oil-immersion technique, first introduced by Grenier et al., was used to eliminate the strong optical aberration of the cylindrically shaped fiber<sup>46,48</sup> and provide a robust, reproducible, and undistorted method for rapid laser exposure to build optical and microfluidic components into integrated 3D optofluidic fiber systems for the first time. The exposures were optimized to form in-fiber waveguides, X-coupler taps<sup>48,94</sup>, FBGs, microholes, mirrors, optofluidic resonators, and reservoirs. These components were, in turn, combined and integrated into multi-component 3D optofluidic fiber sensors as demonstrated by (1) fluorescence excitation and detection in microfluidic channels formed through the SMF core waveguide, (2) highly contrasting reflection spectra from a Fabry Perot interferometer (FPI) for inline refractometry in coreless fiber, and (3) combinational FPI with FBG sensing for simultaneous refractive index, temperature, and bend sensing with high optical finesse. The demonstration of these varied and multiplexed-devices present the future promise for higher-level integration of cladding photonics and

optofluidics that may be efficiently distributed over long fiber length. Hence, the advanced structuring techniques presented here form the basis for generating more advanced LIF systems for creating in-fiber grating spectrometers, spectral filters, flow-cytometers, biomedical probes and smart catheters that are not currently available in LOCs or LOFs.

## 2 LIF Design and Integration

In building a LIF inside SMF, the coupling of light or the intersecting of microfluidic and optical cavities with the germanium-doped core waveguide was the primary technical challenge that required sub-wavelength alignment precision to minimize optical insertion loss. When opening cavities against the waveguide core, such precision was limited by a faster chemical etching rate in the germanium-doped fiber core than in the fused silica cladding as previously reported<sup>22,95</sup> and thereby led to deleterious negative lensing effects from the concave etched core waveguide into the cavity. To counter such differential etching, open channels and cavities were also formed inside an all-fused silica coreless optical fiber to meet with buried laser-formed waveguides, and thus form undistorted fiber-based optofluidic devices which could, in turn, be fused to SMF for seamless inline probing.

A variety of integrated LIF sensors are proposed here for refractive index, temperature, bend, and strain sensing that may be readily monitored in transmission or reflection mode with standard broadband optical sources and optical spectrum analyzers (OSAs) that are interconnected through traditional fiber coupling and optical circulator techniques as shown schematically in Fig. 1-a. A multifunctional fiber sensor design is proposed as shown schematically in Fig. 1-b with three ports for coupling or extracting the probing light. The first in-fiber element is a X-coupler that demultiplexes the light signal entering from the left for probing both the central SMF core waveguide and the laser-formed cladding waveguide. Following the core waveguide, the first element probed is a traversing through-hole that may be filled with fluorescent dyes, liquids, or gases. Hence, the core waveguide may excite and simultaneously capture fluorescent signals generated within the hole or be used for conventional absorption spectroscopy. The microhole sensor is followed by a laser-formed FBG (Fig. 1-b middle) as positioned concentric with the SMF core waveguide for temperature and / or axial strain measurement and is insensitive to fiber bending strain. Following the FBG is a fusion-spliced coreless fiber (Fig. 1-b right) that provides low insertion loss-coupling (1.75 dB<sup>47</sup>) from the SMF core into the laser-formed waveguide to probe an inline FPI for refractive index sensing of the opened optical resonator. For the centrally positioned waveguide, the FPI response will also be insensitive to fiber bending strain.

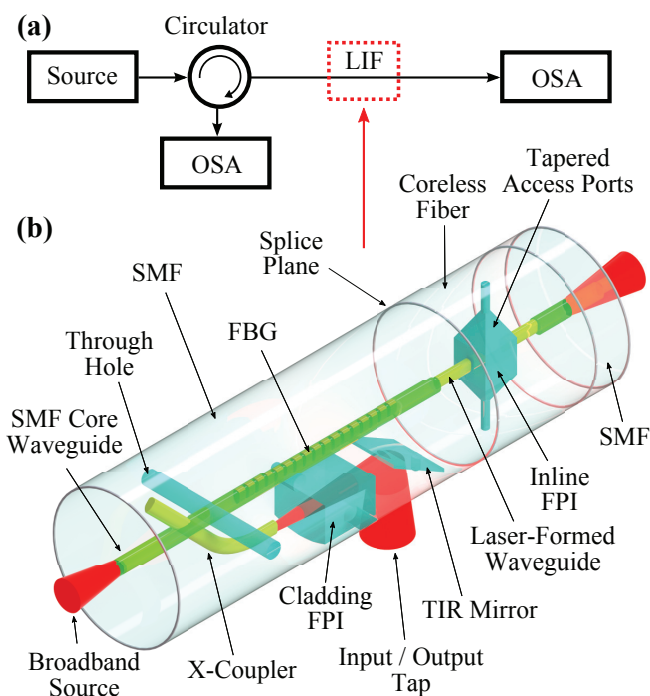


Fig. 1: (a) Optical characterization schematic for simultaneous probing of multiple LIF sensing elements. A broadband optical source is coupled through an optical circulator into the SMF core waveguide. Transmission and reflection spectra are measured with an OSA. (b) Schematic of the proposed LIF sensing elements: (1) a through-hole traversing across the SMF core waveguide for fluorescence detection or absorption spectroscopy, (2) a FBG concentric to the SMF core waveguide for temperature or strain detection, (3) an inline FPI in a coreless optical fiber probed by laser-formed waveguides concentric to the spliced SMF's core for refractive index or pressure sensing, and (4) a X-coupler tap and laser-formed waveguide for probing a cladding FPI for refractive index, pressure, or bend sensing. TIR mirrors are used to either tap light into or out of the fiber cladding for an alternative probing method or for scrubbing undesired cladding modes.

Following the second waveguide branch, the cross-coupler feeds the input light along the curved laser track to define a core waveguide tap and enables efficient optical probing of a cladding-embedded FPI device for refractive index and fiber bend sensing (Fig. 1-b bottom). For the input-output taps, total internal reflecting (TIR) mirrors<sup>96</sup> are embedded within the fiber cladding (Fig. 1-b bottom) to redirect light radially inward from external sources or radially outward from the waveguide to free-space diagnostics, and may also serve to scrub undesired fiber cladding modes that may interfere with spectra generated from downstream LIF sensing elements that otherwise increase the signal-to-noise ratio. A minimum 43.2° incident angle is required in fused silica to initiate TIR.

Collectively, these radially offset and longitudinally distributed sensing elements may be positioned flexibly within and along the optical fiber and be probed simultaneously in reflection (Fig. 1-b left), transmission (Fig. 1-b right) or radially outward with the TIR mirror (Fig. 1-b bottom) for multiplexed measurement of fluorescence, temperature, strain, pressure, fluid refractive index, and fiber bending, all within the compact and flexible LIF platform.

The FBG element in Fig. 1-b is laser-fabricated point-by-point following previous work<sup>97-99</sup> and is briefly reviewed by Liao and Wang<sup>100</sup>. Here, we follow Grenier et al.<sup>46,48,101</sup> to write a single FBG concentric to the SMF core waveguide (Fig. 1-b) to introduce a stopband within the recorded reflection and transmission spectra. The FBG is immune to external liquids, electric fields, and fiber bending and follows the well-known FBG temperature and strain response of<sup>102</sup>

$$\frac{\Delta\lambda}{\lambda_B} = \left(1 - p_e\right)\varepsilon + \left(\alpha + \frac{\zeta}{n}\right)\Delta T, \quad (1)$$

where  $\Delta\lambda$  is the Bragg wavelength shift,  $\lambda_B$  is the Bragg wavelength,  $\varepsilon$  is the applied strain,  $\Delta T$  is the temperature variation,  $p_e = 0.2$  is the dimensionless effective strain-optic constant,  $\alpha = 0.55 \times 10^{-6} \text{ C}^{-1}$  is the linear thermal expansion coefficient for fused silica,  $\zeta = 8.6 \times 10^{-6} \text{ C}^{-1}$  is the thermo-optic coefficient for fused silica at  $1.5 \mu\text{m}$  wavelength, and  $n = 1.445$  is the refractive index for fused silica at  $1.5 \mu\text{m}$  wavelength<sup>103</sup>. The FBG serves as a reference to compensate for temperature- or strain-dependent fluctuations observed from other LIF sensing elements shown in Fig. 1-b that we follow according to the calculated sensitivity response as summarized in Table 1 for  $\lambda_B = 1.55 \mu\text{m}$ . Alternatively, multiple FBGs have been previously written in the fiber cladding (not shown) as demonstrated by Lee et al.<sup>47</sup> to completely measure applied strain, temperature, and the 3D fiber shape in real-time.

Table 1: Sensitivity responses at  $\lambda_B = 1.55 \mu\text{m}$  wavelength as calculated for FBGs and FPIs to measure strain, temperature, and refractive index. Values for the FPI are  $L = 30 \mu\text{m}$ ,  $m = 38$  for air, and  $m = 51$  for water.

	Strain ( $\text{pm}/\mu\text{e}$ )	Temperature ( $\text{pm}/^\circ\text{C}$ )	Refractive Index ( $\text{nm}/\text{RIU}$ )
FBG	1.24	10	-
FPI		0.01 (Air)	40 (Air)
Free Spectral Range	0.04	0.4 (Water, $0^\circ\text{C}$ ) 5 (Water, $100^\circ\text{C}$ )	22 (Water)
FPI Resonance Peak	1.58	0.6 (Air) 23 (Water, $0^\circ\text{C}$ ) 290 (Water, $100^\circ\text{C}$ )	1580 (Air) 1175 (Water)

The inline FPI of Fig. 1-b presents an open optical resonator that relies on Fresnel reflection to generate interference responses in the reflection and transmission spectra as probed by the laser-formed core waveguide in coreless fiber. When the cavity undergoes heating, axial strain, or medium changes (i.e. fluids or gases), the free spectral range ( $FSR$ ) and peak transmission wavelength ( $\lambda_T$ ) shift according to the well-known FPI Airy function with

$$FSR = \frac{\lambda_T^2}{2n[\Delta T, \varepsilon]L[\Delta T, \varepsilon] + \lambda_T} \quad (2)$$

$$\lambda_T = \frac{2n[\Delta T, \varepsilon]L[\Delta T, \varepsilon]}{m}, \quad (3)$$

where  $n[\Delta T, \varepsilon]$  is the refractive index of the medium inside the FPI cavity,  $L[\Delta T, \varepsilon]$  is the FPI cavity length, and  $m$  is a natural number. Equations (2) and (3) may therefore be used for the present purpose of refractive index, temperature, or strain sensing along the fiber center, or similarly within the fiber cladding for off-axis bend and refractive index measurements. Temperature and refractive index sensing is explored here with a small cavity length of  $30 \mu\text{m}$  that minimizes diffraction loss and multimode interference against higher device sensitivity and sensing resolution. The calculated FPI sensitivities for strain, temperature, and refractive index at this  $30 \mu\text{m}$  length are summarized in Table 1 for air and water at freezing and boiling temperatures near the  $1.55 \mu\text{m}$  wavelength. The expected FPI  $FSR$  sensitivities are small in comparison with the FBG sensitivities (Table 1), but are appropriate for calibrating large scale changes to refractive index on the order of  $\Delta n \approx 10^{-2}$  according to Equation (2). However, more precise spectral means to follow shifts in a single FPI resonant peak ( $\lambda_T$  of Equation 3) offer significantly higher sensitivities ( $50\times$ ) and are therefore more appropriate for high-resolution refractive index, temperature, or strain sensing applications.

The structural design of all cavities and channels frequently require tapered or small angled edges (Fig. 1-b right) as was shown by Ho et al.<sup>92</sup> to ensure unrestricted capillary flow of fluids and prevent trapping of air bubbles<sup>104-107</sup>. The cross-sectional area of the cavities is further kept small (i.e.  $30 \times 30 \mu\text{m}^2$ ) in order to maintain the mechanical strength of the  $125 \mu\text{m}$  diameter optical fiber.

### 3 FLICE Fabrication and LIF Methods

The advanced laser processes optimized here enable the fabrication of highly functional LIF components that offer rapid prototyping capabilities into fully integrable 3D optofluidic systems. A commercial femtosecond fiber laser (IMRA America  $\mu\text{Jewel D-400-VR}$ ) with  $1045 \text{ nm}$  center wavelength,  $1 \text{ MHz}$  repetition rate,  $200 \text{ fs}$  (Lorentzian FWHM) pulse duration and ( $M^2 =$ )  $1.35$  beam quality was used for device fab-

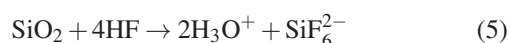
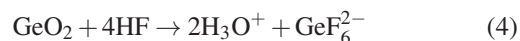
rication in optical fiber. The optical delivery system was previously described by Shah et al.<sup>34</sup> and used (1) an acoustic-optic-modulator for on-off laser switching and Bragg grating modulation, (2) a lithium triborate nonlinear crystal for second harmonic generation to 522 nm wavelength, (3) air-bearing linear motion stages (Aerotech ABL1000, ALS130) for sample positioning and translation, and (4) a CCD camera for laser alignment and imaging of the target surface. Grenier et al.<sup>46,48</sup> and Cheng et al.<sup>94</sup> further describe the mounting of the glass optical fiber (Corning SMF28e) to the translation stages after first removing the polymer jacket by mechanical stripping and acetone wiping.

The formation of nanograting etching templates, FBGs, and optical waveguides were all made under focusing with a 100 $\times$ , 1.25 NA microscope objective and using refractive index oil ( $n = 1.464$ , LRIA-165 Cargille Laboratories) that was matched to that of fused silica to eliminate spherical aberration from the air-cladding interface<sup>46,48</sup>. This facilitated aberration-free focusing of the femtosecond laser light within optical fiber for distortion-free writing of 3D optical and microfluidic devices at any arbitrary position in the fiber cross-section. Laser exposures were first optimized in bulk glass for (1) minimizing propagation losses of single mode waveguides operating at 1.55  $\mu\text{m}$  wavelength, (2) maximizing processing speed of microfluidic channel interiors, and (3) minimizing wall roughness of channel boundaries. These optimized exposure recipes as summarized in Table 2 were then applied to the structuring of the pure fused silica cladding of SMF and found to yield similarly optimized structures. The laser nanograting templates were etched with 5% aqueous HF (Aeros Organics) solution for approximately 1 hour to fully open into microfluidic channels and open cavities at a rate of  $\sim 300 \mu\text{m/hr}$ .

Waveguides were fabricated with the writing laser polarization aligned parallel with the scan direction. In this way, the laser-formed nanograting planes were aligned perpendicular to the optical axis of the waveguides to reduce waveguide birefringence<sup>42</sup> and to inhibit HF etching into the waveguide<sup>92,107</sup>. The waveguides formed according to the exposure in Table 2 yielded a mode size of  $7.64 \times 6.34 \mu\text{m}^2$  ( $1/e^2$  intensity radius), a propagation loss of 0.5 dB/cm and a 0.3 dB loss per facet. To further reduce the opportunity for acid etching into the waveguide, the laser waveguide track was terminated approximately 6  $\mu\text{m}$  from microfluidic channel walls. Conversely, the walls of reservoirs, large channels, and optical resonators were formed by arrays of laser modification tracks with the writing laser polarization selected to align perpendicular to the scan direction and thereby present the smoothest wall profile<sup>92,107</sup> orthogonally against the probing waveguide direction. To speed processing time, high-energy (60 nJ) fast and low-energy (20 nJ) slow scan speeds were preferentially applied to define the interior and boundary zones, respectively, of the channels and cavities for the advan-

tage of forming smooth side walls (slow scan) around a rapidly etchable channel interior (fast scan). Access ports were fabricated with a single “bottom-up” scan to delay the laser focusing into the immersion oil which otherwise generated bubbles that distorted the laser propagation path when scanning downward. To speed the formation of larger volume reservoirs, laser-scanning tracks were formed into intersecting orthogonal planes that, upon chemical etching, released fused silica cubes of  $25 \times 25 \times 25 \mu\text{m}^3$  volume to shape the reservoir<sup>107</sup>. To improve the structural uniformity of laser modification tracks against a scanning directional dependence commonly known as a quill effect<sup>108</sup>, all laser scans were made along only one optimal scan direction for each orthogonal axis.

A much faster intrinsic etching rate in the germanium-doped core of SMF over the pure fused silica cladding follows the respective reactions<sup>109,110</sup>



that are driven by the smaller dissociation energy of the Ge–O bond (660.3 kJ/mol) over the Si–O bond (799.6 kJ/mol) bond<sup>25</sup>. The formation of nanogratings into the core waveguide volume is less controllable than in the cladding due to this undesirable Ge–O etching<sup>22,95</sup> that leads to the formation of concave surface profiles and undesirable negative lensing loss where microfluidic templates meet with the SMF core waveguide. Microfluidic templates were therefore restricted from intersecting the core waveguide to provide for low-loss optofluidic devices.

For fluorescence detection, a  $10^{-3}$  M rhodamine B (Bio-Chemika, No. 83689) solution was drawn by capillary force to fill the through-hole of Fig. 1-b (left). A 535 nm wavelength optical source (Lasermate M206309) was launched into the fiber core waveguide to generate fluorescence which was optically characterized in the forward propagation direction by an OSA (Ando AQ6315A) operating at visible wavelengths. Temperature, refractive index, and fiber bending measurements were recorded simultaneously amongst the optofluidic components of the fiber sensor in Fig. 1-b by launching a 1530-1610 nm wavelength light from a broadband source (Photonicetics Tunics-BT) into the core waveguide and characterized in transmission or reflection through an optical circulator (Thorlabs 6015-3-FC) by the OSA (Ando AQ6317B) as shown in Fig. 1-a. The fiber sensor was placed in an oven (Despatch H17 20094389) to calibrate the FBG wavelength shift with temperature to 1 $^\circ\text{C}$  precision. The LIF was also curved to fit inside a beaker filled with distilled water and heated with a hotplate (Fisher Scientific Isotemp 1-800-49SH) to provide simultaneous measurement of the temperature and refractive index of water.

Table 2: Laser parameters for writing waveguides and microfluidic templates in bulk fused silica and optical fiber.

	Waveguide	X-Coupler	FBG (SMF Core Waveguide)	Microfluidic Channel Interior	Microfluidic Channel Boundary	Microfluidic Access Port
Pulse Energy	70 nJ	70 nJ	20 nJ	60 nJ	20 nJ	30 nJ
Scan Speed	0.1 mm/s	0.1 mm/s	0.1 mm/s	2.5 mm/s	0.3 mm/s	0.3 mm/s
Track Separation	-	-	-	1 $\mu\text{m} \times 1 \mu\text{m}$	1 $\mu\text{m} \times 1 \mu\text{m}$	-
Duty Cycle	-	-	60%	-	-	-
Turning Radius	-	40 mm	-	-	-	-

## 4 LIF Sensing Results and Applications

### 4.1 Microfluidic Holes and 3D Networks

The first concept examined here for a LIF sensing element is a traversing through-hole to intersect the core waveguide of SMF for in-fiber fluorescence characterization. After widely varying the laser exposure condition, the smoothest and least-tapered through-holes were found in a single “bottom-up” laser scan for the exposure in the “microfluidic access port” column of Table 2 and followed with our standard HF chemical etching step (5% aqueous HF for 1 hour). The optical micrographs of Fig. 2-a and 2-b show smooth and crack-free holes to have formed through the full 125  $\mu\text{m}$  cross-section of the fiber, maintaining a highly uniform 5  $\mu\text{m}$  diameter for a large  $25\times$  aspect ratio. The hole provided a strong capillary force to draw fluorescent solutions to fully fill the hole volume and enable absorption or fluorescence spectroscopic probing by directing and detecting light solely along the SMF core waveguide.

The photograph of Fig. 2-c views a single-holed fiber where yellow fluorescence of 570 nm wavelength has been excited in rhodamine B dye from the microhole-waveguide intersection by the green light guided into the fiber core waveguide. The 535 nm wavelength light source is also seen in the image to scatter from weakly guided higher order waveguide modes as well as from stripping of cladding-guided light by the external droplet. The 570 nm fluorescence was visible by eye (Fig. 2-c) and could be captured in the forward waveguide propagation direction together with the excitation light (535 nm) to record the spectrum as shown in Fig. 2-d. Much improved contrast of the absorption spectrum is anticipated with a transverse or backwards observation direction, for example, as noted by the isolation and dominance of the yellow fluorescence spot at the hole position in the photo of Fig. 2-c.

A closer examination of the waveguide-hole intersection in Fig. 2-c reveals  $\sim 1\text{-}3 \mu\text{m}$  of over-etching from the laser-defined hole into the germanium-doped waveguide core that follows the differential etching expectation inferred from the lower dissociation energy for Equation (4) versus Equation (5). This concave contour causes a negative lensing effect

that led to larger insertion loss than expected from a straight cylindrical hole. Similar concave profiles were observed when attempting to form planar etching walls across the SMF core waveguide. However, highly flat and smooth walled structures could be opened to form distortion-free optical cavity walls anywhere in the SMF cladding or coreless optical fiber, which could then be probed by laser-formed waveguides. The distortion-free writing of microfluidic networks inside coreless fiber is noted by the straight blind-hole of Fig. 2-f, and the more elaborate 3D system as shown schematically in Fig. 2-g and by the micrograph in Fig. 2-h. For this 3D representative example, a single embedded microchannel separates into four radial arms that may each be independently probed by laser-formed waveguides (not shown). These structures may be envisioned over long lengths of optical fiber that exploit the benefits of undistorted laser writing with the oil-immersion lens and interconnect optical waveguides with microchannels in straight, circular, or arbitrarily complex shapes.

### 4.2 Optical Resonators

The formation of microfluidic reservoirs and optical resonators may be arbitrarily shaped and positioned into optical fiber to enable efficient fluidic access and exchange from external sources as well as to provide refracting or TIR surfaces that broaden the opportunities for integrating micro-optical devices such as lenses and mirrors. An example of a fiber reservoir is shown in the optical micrographs of Fig. 3-a and 3-b, where 20 cubic blocks ( $25 \times 25 \times 25 \mu\text{m}^3$ ) were laser patterned and released upon HF etching to open into a  $50 \times 50 \times 125 \mu\text{m}^3$  reservoir. An important objective is the formation of optically smooth interfaces that can minimize optical scattering loss<sup>111</sup> when probed by light and also reduce the Reynolds number to ensure laminar flow benefits<sup>112</sup>. An atomic force microscopy profile of the reservoir sidewall (Fig. 3-a) over a  $4 \times 4 \mu\text{m}^2$  area is shown in Fig. 3-c to reveal a small 12 nm (rms) surface roughness that corresponds to a good  $\lambda/130$  local flatness for the present 1550 nm wavelength study. Such smoothness relies on the assembly of nanograting planes over many laser pulses applied in optimally spaced and parallel scanning tracks. The nanoplanes were preferen-

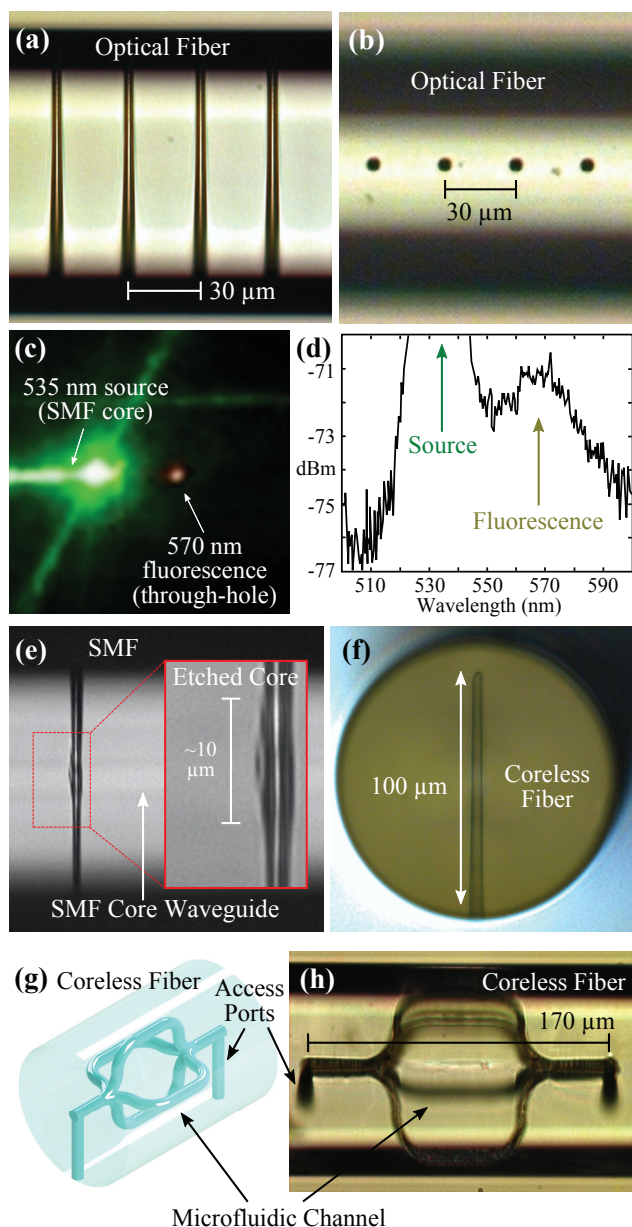


Fig. 2: Optical micrographs of through-holes traversing across SMF and shown from the (a) side and (b) top view. (c) A 535 nm wavelength light source propagates along the SMF core waveguide and excites rhodamine B fluorescence in the traversing 5  $\mu\text{m}$  diameter through-hole. (d) Fiber transmission spectrum showing both source and excited fluorescence at 535 nm and 570 nm wavelength, respectively, for the through-hole in (c). (e) Side view micrograph of SMF showing chemical over-etching ( $\sim 1\text{--}3\ \mu\text{m}$ ) from the traversing laser tracks into the germanium-doped fiber core. (f) End view of a traversing blind hole in coreless fiber. (g) Schematic and (h) optical micrograph of a representative 3D microfluidic network embedded within a coreless optical fiber of 125  $\mu\text{m}$  diameter. A single microchannel is split into four separate radial arms that may each be independently probed by laser-formed waveguides (not shown).

tially aligned perpendicular to the writing laser's polarization as noted previously in bulk glass processing<sup>92,107</sup>. Selective control over the writing laser exposure and polarization therefore opens new broad approaches for forming 3D microfluidic networks of various sizes (i.e. holes in Fig. 2-a) and flexible 3D shapes (i.e. Fig. 2-h) that may be opened into and interconnected with smooth-walled structures such as the reservoir in Fig. 3-a and further with waveguides, mirrors, and optical resonators as explored below.

The benefit of forming optically smooth surfaces is first examined for a rectangular microcavity to create the novel possibility of micro-optical resonators such as FPIs that may be optically interrogated by laser-formed waveguides. Nanograting templates defining an optical resonator were formed by laser-scanning two-dimensional arrays of overlapping laser tracks that connected with overlapping access ports, whose accumulative modification volume was susceptible to HF etching. Laser writing of both waveguides and resonators into coreless fiber, as shown schematically in Fig. 1-b, was favored for generating optically smooth resonators that avoided the undesired SMF core waveguide over-etching. Figure 3-d shows a top view optical micrograph of a 5  $\mu\text{m}$  wide FPI traversing across coreless fiber and intersecting two laser-formed waveguides that are not visible under the present top lighting condition. Figures 3-e and 3-f image the same FPI from the side view to reveal the laser-formed waveguides and smooth channel boundaries under back- and front-lighting, respectively. Figure 3-g shows the measured transmission and reflection spectra recorded through laser-formed waveguides that intersect a similar 29.95  $\mu\text{m}$  wide air-filled FPI, yielding the expected  $FSR = 40.4\ \text{nm}$ . The maximum measured transmission and reflection values of 0.5 dB and 10.2 dB, respectively, match well with calculated FPI values of 0.45 dB and 9.63 dB, respectively, expected after also accounting<sup>113</sup> for diffraction loss across the resonator gap. The fringe contrasts of approximately 0.5 dB and 15 dB for transmission and reflection spectra, respectively, are also consistent with calculated values of 0.445 dB and 20.5 dB. However, backscatter of light lost into fiber cladding modes caused the lower contrast in the reflection spectrum. A waveguide scattering loss of 0.5 dB/cm and facet coupling loss of 0.3 dB were normalized out of the reported spectra for the present 10 mm long sample.

The demonstration of FPIs in Fig. 3-d to 3-g opens the significant opportunity of refractive index sensing of fluids from directly within optical fiber. Figure 3-h shows an optical micrograph of a 27.2  $\mu\text{m}$  long FPI, inline with a laser-formed waveguide, that provides a 45° taper angle to assist with capillary flow of the sensing fluid as schematically illustrated in Fig. 1-b. Spectral recordings of the FPI when filled with methanol, acetone, and isopropanol were similar to the air-filled spectra in Fig. 3-g, but with a reduced visibility contrast and having a smaller  $FSR$  as anticipated by the refractive in-

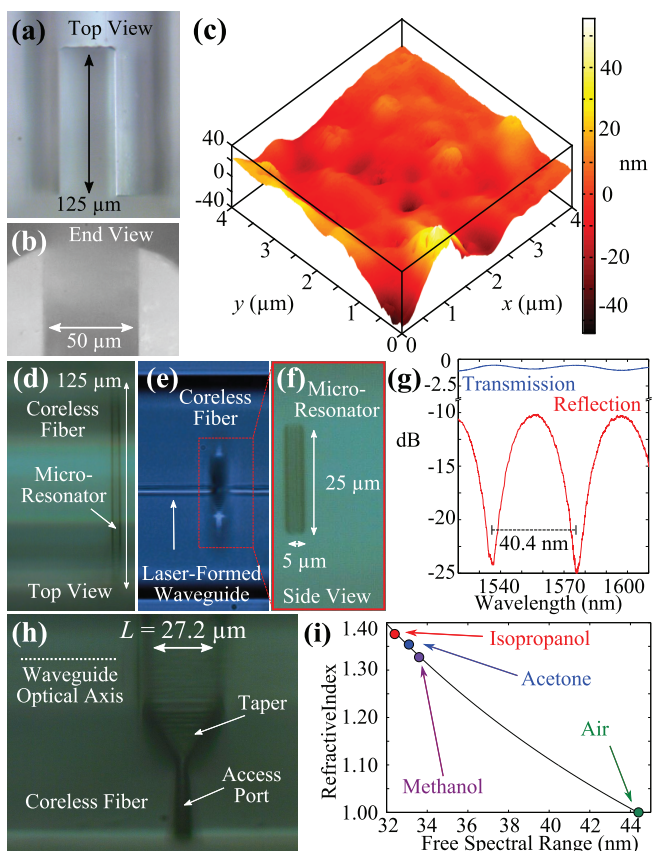


Fig. 3: (a) Top and (b) end view optical micrographs of a cleaved microfluidic reservoir fabricated in optical fiber. (c) Atomic force microscopy surface profile of a reservoir sidewall over  $4 \times 4 \mu\text{m}^2$  area indicating a 12 nm (rms) surface roughness. (d) Side view optical micrograph image with front illumination of a  $5 \mu\text{m}$  wide optical resonator formed inside coreless fiber. (e) The probing laser-formed waveguides imaged under back illumination of the same resonator of (d) when rotated by  $90^\circ$ . (f) Magnified optical micrograph of the same resonator of (e) with front illumination. (g) Transmission (blue) and reflection (red) spectra recorded in-fiber through a similar air-filled  $29.95 \mu\text{m}$  wide resonator showing the expected FPI interference fringes of approximately 0.5 dB and 14 dB contrast, respectively, and  $FSR = 40.4 \text{ nm}$ . (h) Inline FPI as schematically shown in Fig. 1-b with a  $45^\circ$  taper angle to the connected access port. (i) Refractive index values of various alcohols and air as spectrally measured ( $FSR$ ) from the FPI shown in (h) and calculated from Equation (2) with  $L = 27.2 \mu\text{m}$  and  $\lambda = 1.575 \mu\text{m}$ .

dex responses in Equations (2) and (3). Figure 3-i plots the refractive index value evaluated for each fluid and air as inferred from Equation (2) for the values of  $L = 27.2 \mu\text{m}$  and  $\lambda = 1.575 \mu\text{m}$ . These refractive index values agree within  $\pm 0.5 \times 10^{-3}$  of the known values<sup>54</sup>. Considering our  $\pm 0.25 \text{ nm}$  precision in identifying the FPI reflection peaks, we infer a maximum 43 nm/RIU sensitivity from the slope in Equations

(2) (at  $n = 1.0$ ) that indicates a maximum refractive index accuracy of  $10^{-2}$  for the present FPI. Alternatively, a significantly better value of  $3 \times 10^{-4}$  is found for the precision when directly following the wavelength shift of a single FPI resonance trough which scales much faster than  $FSR$ , providing 1580 nm/RIU sensitivity as calculated from Equation (3) for  $1.575 \mu\text{m}$  wavelength. These sensitivity values may be increased by lengthening the FPI cavity, but larger diffraction losses will eventually weaken the visibility contrast and decrease the overall sensing resolution. To fully optimize a longer FPI cavity length, one may consider the development of waveguides with larger waveguide mode size as well as the introduction of curved FPI surfaces that focus the beam and reduce diffraction loss to provide stronger spectral visibility contrast.

### 4.3 Integrated LIF Sensors

We now explore the integration of multiple optical and microfluidic sensing elements that follow the design presented in Fig. 1-b to demonstrate simultaneous sensing capabilities. A schematic of the laser fabricated LIF is shown in the end and side ( $\alpha = 0^\circ$ ) views of Fig. 4-a and 4-b, respectively, where a laser-formed FBG was written concentric to the SMF core waveguide for temperature sensing as shown in the optical micrograph of Fig. 4-c. Simultaneously, a laser-formed X-coupler tapped light from the SMF core waveguide to probe a FPI embedded within the fiber cladding for refractive index sensing of fluids filling the FPI cavity of  $27.1 \mu\text{m}$  length. A  $2^\circ$  inclination angle was used between the SMF core and laser-formed waveguide to define a balanced 3 dB X-coupler as shown in the optical micrograph of Fig. 4-d. This angle provided a strong 40% tapping efficiency (one way) for probing of the FPI, leaving  $\sim 40\%$  in the core waveguide to probe the FBG. An estimated 20% of the incoming light was lost at the X-coupler into cladding modes. Finally, a TIR mirror was positioned after this cladding FPI to eject light scattered and lost into fiber cladding modes. The combination of laser-formed waveguide, cladding FPI, and TIR mirror are shown in the optical micrographs from side views rotated by  $\alpha = 0^\circ$  (Fig. 4-e) and  $\alpha = 75^\circ$  (Fig. 4-f) with respect to the image in Fig. 1-b. The structures in Fig. 4-e closely resemble the design structure of Fig. 4-b. Red light launched into the fiber core waveguide was seen to only be weakly scattered from the FPI walls in Fig. 4-f and then became strongly ejected by the TIR mirror. The mirror also served as an efficient out coupler for side tapping of the FPI transmission spectrum.

Reflection spectra generated by the LIF sensor are shown in Fig. 5-a for an air-filled optical resonator with the fiber straight and non-stressed, and presented for a range of temperatures from  $40^\circ\text{C}$  to  $200^\circ\text{C}$ . The 40% tapping by the X-coupler facilitated simultaneous probing of the 4 mm long FBG with

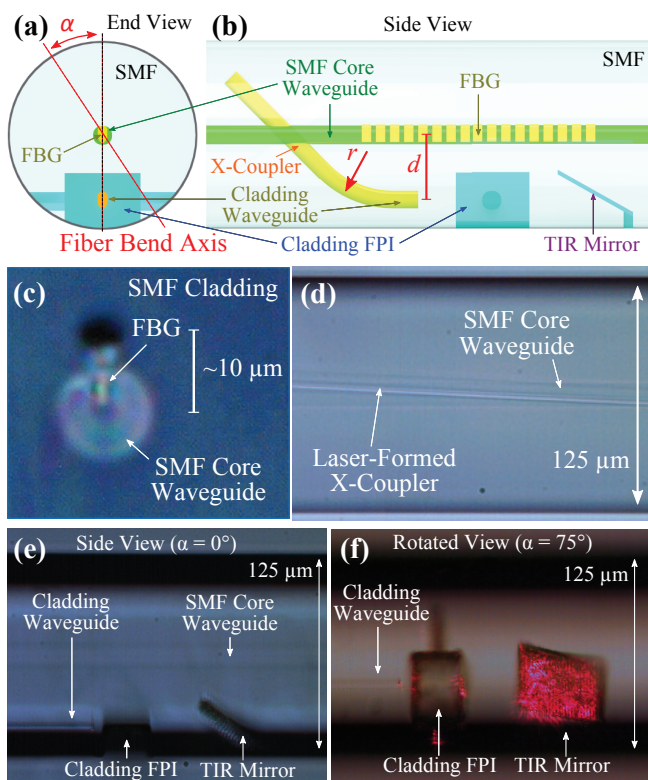


Fig. 4: Cross-sectional (a) end and (b) side ( $\alpha = 0^\circ$ ) views of an optical-microfluidic integrated LIF sensor. A weak Bragg grating is laser written inside the SMF core waveguide for FBG temperature sensing, while a laser-formed X-coupler taps light out of the SMF core waveguide into a cladding waveguide for probing of the cladding FPI. A tilted TIR mirror is embedded after the FPI to strip out light scattering into cladding modes. Optical micrographs of the laser-formed (c) Bragg grating, (d) X-coupler, and (e) cladding FPI and TIR mirror ( $\alpha = 0^\circ$ ) embedded inside SMF that together form the integrated LIF sensor. (f) A rotated ( $\alpha = 75^\circ$ ) view of (e) when showing scattering and ejection of red light that was coupled into the SMF core waveguide.

the cladding FPI (27.1  $\mu\text{m}$  cavity length). The FBG manifested in a narrow (0.4 nm) and strong (13 dB) stopband at 1550.6 nm wavelength that rose above a highly contrasting FPI reflection interference spectrum. For the present FPI design, the  $FSR$  of 44 nm and the 12 dB visibility did not lead to a measurable shift of spectral resonances across this temperature range (i.e.  $\Delta\lambda = 0.1$  nm over  $\Delta T = 160^\circ\text{C}$ ) as expected due to the short air-filled cavity length. On the other hand, the FBG resonances were seen to shift strongly in the inset image of Fig. 5-a and led to a temperature response of 11.1  $\text{pm}/^\circ\text{C}$  when plotted in Fig. 5-b that agreed with the expected sensitivity as presented in Table 1. Owing to the central-axis location, this FBG may therefore serve as a thermometer that will

not be influenced by fiber bending or the addition of fluids into the microcavities.

The spectrum in Fig. 5-a shows 2 to 6 dB resonances on the short wavelength side of the FBG ( $\lambda < 1550$  nm) that originate from a combination of effects: (1) cladding mode light forward scattered by the X-coupler at all wavelengths, (2) cladding mode light back-coupled by the FBG at wavelengths less than  $\lambda_B$  and picked up by the X-coupler, (3) FPI effects between the X-coupler and FBG that yield the  $FSR \approx 55$  pm fringes in Fig. 5-a inset (associated with the 15 mm FBG to X-coupler separation), and (4) interference between these components of back-coupled cladding light (1 to 3) and light also back reflected by the FPI. These effects reduced the precision in measuring the  $FSR$  of the FPI, particularly due to the noise around the 1535 nm trough in Fig. 5-a. While index matching epoxy could be applied to remove most of these effects, a similar LIF was laser fabricated that shifted the FBG from 1550.6 nm (Fig. 5-a inset) to 1521.5 nm to provide less noisy LIF reflection spectra as shown in Fig. 5-c.

This modified LIF was then bent to various radii from  $R = \infty$  (black spectrum) to  $R = 22$  nm, leading to an observable shift in the FPI resonance troughs at  $\sim 1530$  nm and  $\sim 1565$  nm as observed in the multiplexed reflection spectra of Fig. 5-c for the air-filled FPI. Here, the FBG resonances were noted to remain locked at  $1521.5 \pm 0.02$  nm, reflecting a stable room temperature condition of  $\pm 2^\circ\text{C}$  over all experimental measurements. For these spectra, the fiber was curved along the bend axis (red line) identified in Fig. 4-a with a precision of  $\alpha = 0 \pm 10^\circ$ . The optical axis of the probing laser-formed waveguide was offset by  $d = 35$   $\mu\text{m}$  (Fig. 4-b) that was large enough to avoid coupling with the SMF core waveguide while providing a sensitive measure of the bending induced strain,  $\epsilon$ , according to the well-known equation of

$$\epsilon = \frac{d}{R}. \quad (6)$$

The center wavelength of the reflection troughs were obtained from Fig. 5-c and plotted versus the bend radius and strain in Fig. 5-d to yield a linear strain response of  $2.7 \pm 0.5$   $\text{pm}/\mu\epsilon$ . This exceeded the expected 1.53  $\text{pm}/\mu\epsilon$  sensitivity, possibly owing to a more pliable fiber structure that was weakened by the  $30 \times 30$   $\mu\text{m}^2$  open FPI cavity. The 0.5 nm uncertainty of the FPI resonances in Fig. 5-d may be improved by reducing the  $\Delta\alpha = \pm 10^\circ$  uncertainty in the azimuthal alignment.

The observed FPI strain response is  $\sim 2.5\times$  larger than expected (1.06  $\text{pm}/\mu\epsilon$ <sup>47</sup>) for the case of a FBG positioned at the same offset, but will only offer a poor accuracy of 185  $\mu\epsilon$  in contrast with the 24  $\mu\epsilon$  for the FBG. This arises from the much narrower (25 pm) FBG peak accuracy in contrast with the  $\sim 500$  pm FPI trough (2.7  $\text{pm}/\mu\epsilon$ ) as noted in Fig. 5-d. However, the cladding FPI occupied only a short 27.1  $\mu\text{m}$  fiber length in contrast with the 4 mm long FBG that is attractive

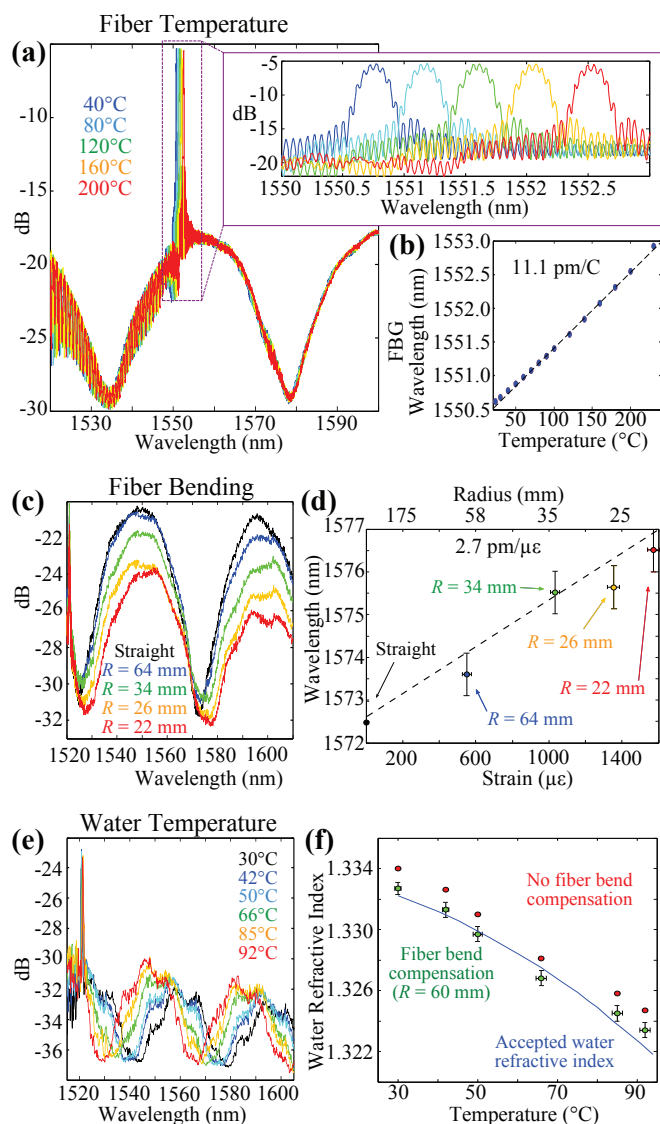


Fig. 5: (a) Reflection spectra recorded from the LIF device schematically shown in Fig. 4 when heated over a temperature range of 40°C to 200°C. The inset spectra shows the wavelength shift of the FBG at different temperatures. (b) Plot of the FBG center wavelength versus temperature, indicating a temperature sensitivity of 11.1 pm/°C. (c) Reflection spectra generated from a similar LIF sensor when bent to various radii about a fiber bend axis aligned at azimuth  $\alpha \approx 10^\circ$  as identified in Fig. 4-a. (d) Wavelength shifts of a FPI reflection trough recorded at different fiber bending radii or strain indicating a 2.7 pm/μϵ strain sensitivity. The horizontal and vertical error bars represent the measurement accuracy for the bending radii and trough center wavelengths, respectively. (e) Reflection spectra of the LIF sensor filled with water heated over the range of 30°C to 92°C. (f) Refractive index of water versus temperature, inferred from wavelength shifts of a trough in the reflection spectrum before (red) and after (green) correcting for the  $R = 60$  nm bending radius of the fiber that agreed with accepted values<sup>54</sup> (blue).

for a higher spatial resolution in dense distributed sensing. A future study that increases the FPI cavity length is attractive for maximizing the overall FPI strain accuracy by balancing a larger sensitivity value against the larger diffraction loss that reduces the spectral visibility contrast.

A similar LIF (Fig. 5-c) was further applied to measure the temperature-dependent refractive index of water over a 30°C to 92°C temperature range. The corresponding 15 nm shift in the measured FPI troughs shown in the reflection spectra of Fig. 5-e clearly confirm a refractive index dependence of the water on temperature that was simultaneously and independently recorded by the FBG resonance shifts. Here, the FBG center wavelength shifted by  $\sim 0.7$  nm over the 30°C to 92°C temperature range. Experimental values of refractive index (red data) were obtained from Equation (3) for FPI values of  $L = 25.1$  μm and  $m = 42$  at the 1580 nm FPI resonant trough and plotted against temperature in Fig. 5-f. These values did not account for radial strain as the LIF sensor was bent to a radius of  $R = 60$  mm to fit in the beaker. A better correspondence (Fig. 5-d) with the accepted refractive index values (blue)<sup>54</sup> was obtained (green) by correcting the fringe shifts for bending strain ( $R = 60$  mm) applied at a best fitted  $\alpha = 10^\circ$  azimuth with good overall accuracy of  $5 \times 10^{-4}$  RIU.

## 5 Discussion and Significance

The opportunity to write 3D optical circuits and microfluidic systems in SMF and coreless optical fiber with femtosecond laser writing and FLICE, respectively, offer several technical and practical advantages over other fiber-based sensors that have been limited to either the fiber cladding surface<sup>13,16–26</sup> or “top-down” geometries<sup>51–59</sup>. Such glass- and fiber-based advantages include immunity to EM interference, compact size, light weight, mechanical flexibility and robustness, chemical inertness, low auto-fluorescence, biocompatibility, high wettability, and large thermal conductivity. Here, representative examples of intersecting microholes (Fig. 2-a and 2-b), fluorescence detectors (Fig. 2-c and 2-d), complex 3D microfluidic networks (Fig. 2-g and 2-h), microfluidic reservoirs (Fig. 3-a and 3-b), optical resonators (Fig. 3-d to 3-g), refractometers (Fig. 3-h and 3-i), FBGs (Fig. 4-c), X-coupler taps (Fig. 4-d), TIR mirrors (Fig. 4-f), and integrated LIF sensors for simultaneous temperature, bend, and refractive index sensing (Fig. 4 and 5) exploit such advantages to collectively verify that femtosecond laser writing and FLICE are powerful tools for the future LIF development.

Distortion-free oil-immersion writing of closely spaced laser modification tracks was found to provide a facile means to position, size, and shape various optically smooth microfluidic structures (12 nm rms, Fig. 3-c) that may now be embedded within fused-silica SMF, coreless, multicore, or photonic crystal fiber. These structures may therefore be ad-

vantageously positioned for probing by the pre-existing core waveguide(s) or further integrated with laser-formed optical circuits (0.5 dB/cm) with low or near-theoretical device insertion loss. The smooth walls were enabled by the preferential alignment of nanogratings formed during laser templating to overcome the rough interfaces previously observed with FLICE-formed LIFs<sup>66,88–91</sup> and hence our devices have significantly improved on the FPI reflectivity, visibility contrast, Q-factor, and sensing resolution. In order to minimize optical losses, it was necessary to avoid positioning of microfluidic templates directly into the germanium-doped SMF core waveguide where concave surface profiles would otherwise form during HF etching (Fig. 2-e) to cause negative lensing effects. In future work, one may attempt to pattern laser tracks to compensate such over etching as well as to introduce microlensing surface profiles at these waveguide positions that reduce overall insertion loss.

The integrated LIF sensor (Fig. 4) presented a combination of four integrated devices with three ports for probing and detection of responses. The  $\sim 1 \mu\text{m}$  precision in positioning the laser within the fiber was instrumental in assembling components with low overall insertion losses (2 dB) that leaves room for higher levels of integration. The prospects for LIF may now significantly advance miniaturization, integration, and parallelization of fiber-based sensing that embraces the full benefits of LOC functionality while going much further to exploit the full 3D cladding geometry for the first time. The widespread fiber platform of today's global telecommunication network is amenable to integration of such optical probes and diagnostics for underpinning future LIF applications that have not been possible to date and offer significant prospects for incorporating grating spectrometers, spectral filters, flow-cytometers, and biometric or environmental sensors. The LIF may therefore enable development of advanced biomedical probes, smart catheters and multi-functional distributed sensing systems that have not been possible in LOCs or LOFs. As femtosecond lasers become more reliable, cheaper, and powerful, their prospects for manufacturing more advanced products will continue to strengthen in a broad range of LIF applications using the building blocks presented here towards numerous applications including efficient information exchange and data multiplexing in telecom networks, smart sensing of catheter bend angles and 3D shapes during medical procedures, compact sensors for security and defense, and low-cost health care products.

## 6 Conclusions

The nanogratings formed in optical fiber during FLICE were exploited for the development of novel LIF sensors. Aberration-free focusing of the writing laser with a high numerical oil-immersion lens provided distortion-free writing

of 3D optical and microfluidic sensing components in arbitrary positions within the fiber core and cladding with unprecedented 12 nm (rms) channel roughness. High precision laser writing therefore facilitated the formation of optical-quality resonators that were readily integrated with laser-formed waveguides, X-coupler taps, FBGs, microholes, mirrors, microfluidic resonators and reservoirs in a 3D fiber platform. Novel fluorescence detectors and high optical quality inline and cladding FPIs were embedded with FBGs for simultaneous refractive index, fiber bending, and temperature sensing. The techniques presented here may enable new directions for designing and fabricating highly functional photonic microsystems and LIF devices for complex laboratory-level diagnostics in the compact, flexible, and standard SMF platform that have not been previously possible with conventional fabrication tools to date.

## 7 Acknowledgments

The authors are grateful for helpful discussions with Jason Grenier on oil-immersion lens focusing into the fiber, and the formation of the cladding waveguides and the fiber X-coupler. The assistance with the fusion splicing of SMF to coreless fiber by Ho Yiu (Kyle) Cheng and laser beam delivery and control by Dr. Jianzhao Li were appreciated. This work was supported by the Natural Sciences and Engineering Research Council of Canada (NSERC) and the Edward S. Rogers Sr. Graduate Scholarship.

## References

- 1 G. M. Whitesides, *Nature*, 2006, **442**, 368–373.
- 2 M. W. L. Watson, M. J. Jebrail and A. R. Wheeler, *Anal. Chem.*, 2010, **82**, 6680–6686.
- 3 D. Psaltis, S. R. Quake and C. Yang, *Nature*, 2006, **442**, 381–386.
- 4 C. Monat, P. Domachuk and B. J. Eggleton, *Nat. Photonics*, 2007, **1**, 106–114.
- 5 D. M. Hartmann, J. T. Nevill, K. I. Pettigrew, G. Votaw, P.-J. Kung and H. C. Crenshaw, *Lab Chip*, 2008, **8**, 609–616.
- 6 P. S. Nunes, N. A. Mortensen, J. P. Kutter and K. B. Mogensen, *Opt. Lett.*, 2008, **33**, 1623–1625.
- 7 J. P. Golden, J. S. Kim, J. S. Erickson, L. R. Hilliard, P. B. Howell, G. P. Anderson, M. Nasir and F. S. Ligler, *Lab Chip*, 2009, **9**, 1942–1950.
- 8 A. Kummrow, J. Theisen, M. Frankowski, A. Tuchscheerer, H. Yildirim, K. Brattke, M. Schmidt and J. Neukammer, *Lab Chip*, 2009, **9**, 972–981.
- 9 Y.-C. Tung, N.-T. Huang, B.-R. Oh, B. Patra, C.-C. Pan, T. Qiu, P. K. Chu, W. Zhang and K. Kurabayashi, *Lab Chip*, 2012, **12**, 3552–3565.
- 10 S. Dochow, M. Becker, R. Spittel, C. Beleites, S. Stanca, I. Latka, K. Schuster, J. Kobelke, S. Unger, T. Henkel, G. Mayer, J. Albert, M. Rothhardt, C. Krafft and J. Popp, *Lab Chip*, 2013, **13**, 1109–1113.
- 11 R. M. Parker, J. C. Gates, D. J. Wales, P. G. R. Smith and M. C. Grossel, *Lab Chip*, 2013, **13**, 377–385.
- 12 J. R. Krogmeier, I. Schaefer, G. Seward, G. R. Yantz and J. W. Larson, *Lab Chip*, 2007, **7**, 1767–1774.
- 13 P. R. Ohodnicki, M. P. Buric, T. D. Brown, C. Matranga, C. Wang, J. Baltrus and M. Andio, *Nanoscale*, 2013, **5**, 9030–9039.

- 14 K. R. Rogers and E. J. Poziomek, *Chemosphere*, 1996, **33**, 1151–1174.
- 15 J. Lopez-Higuera, *Handbook of optical fibre sensing technology*, John Wiley & Sons Ltd., 2002.
- 16 M. Consales, A. Ricciardi, A. Crescitelli, E. Esposito, A. Cutolo and A. Cusano, *ACS Nano*, 2012, **6**, 3163–3170.
- 17 Y. Shevchenko, G. Camci-Unal, D. F. Cuttica, M. R. Dokmeci, J. Albert and A. Khademhosseini, *Biosens. Bioelectron.*, 2014, **56**, 359–367.
- 18 E. Esposito, C. Granata, A. Crescitelli, M. Consales, A. Ricciardi, A. Cutolo and A. Cusano, *Sensors*, 2011 IEEE, 2011, pp. 230–233.
- 19 J. Ma, A. Kos, W. Bock, X. Li, H. Nguyen, Z. Y. Wang and A. Cusano, *J. Lightwave Technol.*, 2012, **30**, 1127–1133.
- 20 A. González-Cano, F.-J. Bueno, Óscar Esteban, N. Díaz-Herrera and M.-C. Navarrete, *Appl. Optics*, 2005, **44**, 519–526.
- 21 Y. Shevchenko, N. U. Ahamad, A. Ianoul and J. Albert, *Opt. Express*, 2010, **18**, 20409–20421.
- 22 T. Zhao, Y. Gong, Y. Rao, Y. Wu, Z. Ran and H. Wu, *Chin. Opt. Lett.*, 2011, **9**, 050602.
- 23 S. Pevec and D. Donlagic, *Opt. Express*, 2011, **19**, 15641–15651.
- 24 A. Veselov, B. Abraham, H. Lemmetyinen, M. Karp and N. Tkachenko, *Anal. Bioanal. Chem.*, 2012, **402**, 1149–1158.
- 25 Y. Gong, Y.-J. Rao, Y. Guo, Z.-L. Ran and Y. Wu, *IEEE Photonic Tech. L.*, 2009, **21**, 1725–1727.
- 26 S. Pevec, E. Cibula, B. Lenardic and D. Donlagic, *IEEE Photonics J.*, 2011, **3**, 627–632.
- 27 A. M. Cubillas, S. Unterkofler, T. G. Euser, B. J. M. Etzold, A. C. Jones, P. J. Sadler, P. Wasserscheid and P. S. Russell, *Chem. Soc. Rev.*, 2013, **42**, 8629–8648.
- 28 F. Korte, S. Adams, A. Egbert, C. Fallnich, A. Ostendorf, S. Nolte, M. Will, J.-P. Ruske, B. Chichkov and A. Tuennermann, *Opt. Express*, 2000, **7**, 41–49.
- 29 C. B. Schaffer, A. Brodeur and E. Mazur, *Meas. Sci. Technol.*, 2001, **12**, 1784.
- 30 Y. Li, K. Itoh, W. Watanabe, K. Yamada, D. Kuroda, J. Nishii and Y. Jiang, *Opt. Lett.*, 2001, **26**, 1912–1914.
- 31 K. M. Davis, K. Miura, N. Sugimoto and K. Hirao, *Opt. Lett.*, 1996, **21**, 1729–1731.
- 32 R. S. Taylor, C. Hnatovsky, E. Simova, D. M. Rayner, V. R. Bhardwaj and P. B. Corkum, *Opt. Lett.*, 2003, **28**, 1043–1045.
- 33 R. Osellame, N. Chiodo, G. Valle, S. Taccheo, R. Ramponi, G. Cerullo, A. Killi, U. Morgner, M. Lederer and D. Kopf, *Opt. Lett.*, 2004, **29**, 1900–1902.
- 34 L. Shah, A. Arai, S. Eaton and P. Herman, *Opt. Express*, 2005, **13**, 1999–2006.
- 35 H. Zhang, S. M. Eaton and P. R. Herman, *Opt. Lett.*, 2007, **32**, 2559–2561.
- 36 S. M. Eaton, H. Zhang, M. L. Ng, J. Li, W.-J. Chen, S. Ho and P. R. Herman, *Opt. Express*, 2008, **16**, 9443–9458.
- 37 M. Ams, P. Dekker, G. D. Marshall and M. J. Withford, *Opt. Lett.*, 2009, **34**, 247–249.
- 38 S. M. Eaton, W.-J. Chen, H. Zhang, R. Iyer, J. Li, M. L. Ng, S. Ho, J. Aitchison and P. R. Herman, *J. Lightwave Technol.*, 2009, **27**, 1079–1085.
- 39 R. M. Vazquez, R. Osellame, D. Nolli, C. Dongre, H. van den Vlekkert, R. Ramponi, M. Pollnau and G. Cerullo, *Lab Chip*, 2009, **9**, 91–96.
- 40 J. C. Ng, C. Li, P. R. Herman and L. Qian, *Opt. Express*, 2012, **20**, 17894–17903.
- 41 L. A. Fernandes, J. R. Grenier, P. R. Herman, J. S. Aitchison and P. V. S. Marques, *Opt. Express*, 2011, **19**, 18294–18301.
- 42 L. A. Fernandes, J. R. Grenier, P. R. Herman, J. S. Aitchison and P. V. S. Marques, *Opt. Express*, 2012, **20**, 24103–24114.
- 43 M. Haque, N. S. Zacharia, S. Ho and P. R. Herman, *Biomed. Opt. Express*, 2013, **4**, 1472–1485.
- 44 R. R. Gattass and E. Mazur, *Nat. Photonics*, 2008, **2**, 219–225.
- 45 A. Martinez, Y. Lai, M. Dubov, I. Khrushchev and I. Bennion, *Electronics Letters*, 2005, **41**, 472–474(2).
- 46 J. R. Grenier, L. A. Fernandes, P. V. Marques, J. S. Aitchison and P. R. Herman, *CLEO:2011 - Laser Applications to Photonic Applications*, 2011, CMZ1.
- 47 K. K. Lee, A. Mariampillai, M. Haque, B. A. Standish, V. X. Yang and P. R. Herman, *Opt. Express*, 2013, **21**, 24076–24086.
- 48 J. R. Grenier, M. Haque, L. A. Fernandes, K. K. C. Lee and P. R. Herman, *Femtosecond laser inscription of photonic and optofluidic devices in fiber cladding*, appearing in Springer Series in Optical Sciences **189**, Ed. G. Marowsky (ISBN 978-1-4937-1178-3), 2014.
- 49 P. J. Bennett, T. M. Monro and D. J. Richardson, *Opt. Lett.*, 1999, **24**, 1203–1205.
- 50 B. Eggleton, C. Kerbage, P. Westbrook, R. Windeler and A. Hale, *Opt. Express*, 2001, **9**, 698–713.
- 51 Y. Wang, D. N. Wang, M. Yang, W. Hong and P. Lu, *Opt. Lett.*, 2009, **34**, 3328–3330.
- 52 Y. Liu, S. Qu and Y. Li, *Opt. Lett.*, 2013, **38**, 335–337.
- 53 Z. L. Ran, Y. J. Rao, W. J. Liu, X. Liao and K. S. Chiang, *Opt. Express*, 2008, **16**, 2252–2263.
- 54 T. Wei, Y. Han, Y. Li, H.-L. Tsai and H. Xiao, *Opt. Express*, 2008, **16**, 5764–5769.
- 55 T. Wei, Y. Han, H.-L. Tsai and H. Xiao, *Opt. Lett.*, 2008, **33**, 536–538.
- 56 Z. Ran, Y. Rao, J. Zhang, Z. Liu and B. Xu, *J. Lightwave Technol.*, 2009, **27**, 5426–5429.
- 57 Y. Wang, M. Yang, D. N. Wang, S. Liu and P. Lu, *J. Opt. Soc. Am. B*, 2010, **27**, 370–374.
- 58 L. Yuan, T. Wei, Q. Han, H. Wang, J. Huang, L. Jiang and H. Xiao, *Opt. Lett.*, 2012, **37**, 4489–4491.
- 59 L. Yuan, J. Huang, X. Lan, H. Wang, L. Jiang and H. Xiao, *Opt. Lett.*, 2014, **39**, 2358–2361.
- 60 A. P. Abel, M. G. Weller, G. L. Duveneck, M. Ehrat and H. M. Widmer, *Anal. Chem.*, 1996, **68**, 2905–2912.
- 61 A. Leung, P. M. Shankar and R. Mutharasan, *Sensor Actuat. B-Chem.*, 2007, **125**, 688–703.
- 62 J. Peterson and G. Vurek, *Science*, 1984, **224**, 123–127.
- 63 A. N. Sloper and M. T. Flanagan, *Appl. Optics*, 1994, **33**, 4230–4240.
- 64 G. Whitenett, G. Stewart, K. Atherton, B. Culshaw and W. Johnstone, *J. Opt. A: Pure Appl. Opt.*, 2003, **5**, S140.
- 65 Y. J. Rao, T. Zhu, X. C. Yang and D. W. Duan, *Opt. Lett.*, 2007, **32**, 2662–2664.
- 66 K. Zhou, L. Zhang, X. Chen, V. Mezentssev and I. Bennion, *International Journal of Smart and Nano Materials*, 2010, **1**, 237–248.
- 67 P. Caldas, J. L. Santos, F. M. Arajo, S. F. O. Silva, O. Frazo and L. A. Ferreira, *Opt. Eng.*, 2008, **47**, 054403–054403–5.
- 68 T. Y. Hu, Y. Wang, C. R. Liao and D. N. Wang, *Opt. Lett.*, 2012, **37**, 5082–5084.
- 69 T. Wei, X. Lan and H. Xiao, *IEEE Photonic Tech. L.*, 2009, **21**, 669–671.
- 70 G. Stewart, W. Jin and B. Culshaw, *Sensor Actuat. B-Chem.*, 1997, **38**, 42–47.
- 71 O. S. Wolfbeis, *Anal. Chem.*, 2004, **76**, 3269–3284.
- 72 Y. Wang, D. N. Wang, C. Wang and T. Hu, *Opt. Express*, 2013, **21**, 14084–14089.
- 73 Y. Shimotsuma, P. G. Kazansky, J. Qiu and K. Hirao, *Phys. Rev. Lett.*, 2003, **91**, 247405.
- 74 C. Hnatovsky, R. S. Taylor, E. Simova, V. R. Bhardwaj, D. M. Rayner and P. B. Corkum, *Opt. Lett.*, 2005, **30**, 1867–1869.
- 75 C. Hnatovsky, R. Taylor, E. Simova, P. Rajeev, D. Rayner, V. Bhardwaj and P. Corkum, *Appl. Phys. A-Mater.*, 2006, **84**, 47–61.
- 76 W. Yang, E. Bricchi, P. G. Kazansky, J. Bovatsek and A. Y. Arai, *Opt. Express*, 2006, **14**, 10117–10124.

- 77 S. Richter, M. Heinrich, S. Dring, A. Tnnermann and S. Nolte, *Appl. Phys. A-Mater.*, 2011, **104**, 503–507.
- 78 F. Liang, R. Vallée and S. L. Chin, *Opt. Express*, 2012, **20**, 4389–4396.
- 79 Y. Bellouard, A. Said, M. Dugan and P. Bado, *Opt. Express*, 2004, **12**, 2120–2129.
- 80 S. Kiyama, S. Matsuo, S. Hashimoto and Y. Morihira, *J. Phys. Chem. C*, 2009, **113**, 11560–11566.
- 81 R. W. Applegate Jr., J. Squier, T. Vestad, J. Oakey, D. W. M. Marr, P. Bado, M. A. Dugan and A. A. Said, *Lab Chip*, 2006, **6**, 422–426.
- 82 D. Hwang, M. Kim, K. Hiromatsu, H. Jeon and C. Grigoropoulos, *Appl. Phys. A-Mater.*, 2009, **96**, 385–390.
- 83 V. Maselli, J. R. Grenier, S. Ho and P. R. Herman, *Opt. Express*, 2009, **17**, 11719–11729.
- 84 M. Kim, D. J. Hwang, H. Jeon, K. Hiromatsu and C. P. Grigoropoulos, *Lab Chip*, 2009, **9**, 311–318.
- 85 F. Bragheri, L. Ferrara, N. Bellini, K. C. Vishnubhatla, P. Minzioni, R. Ramponi, R. Osellame and I. Cristiani, *J. Biophotonics*, 2010, **3**, 234–243.
- 86 R. Osellame, H. Hoekstra, G. Cerullo and M. Pollnau, *Laser & Photonics Reviews*, 2011, **5**, 442–463.
- 87 B.-B. Xu, Y.-L. Zhang, H. Xia, W.-F. Dong, H. Ding and H.-B. Sun, *Lab Chip*, 2013, **13**, 1677–1690.
- 88 K. Zhou, Y. Lai, X. Chen, K. Sugden, L. Zhang and I. Bennion, *Opt. Express*, 2007, **15**, 15848–15853.
- 89 H. Fu, K. Zhou, P. Saffari, C. Mou, L. Zhang, S. He and I. Bennion, *IEEE Photonic Tech. L.*, 2008, **20**, 1609–1611.
- 90 J. Petrovic, Y. Lai and I. Bennion, *Appl. Optics*, 2008, **47**, 1410–1416.
- 91 K. Zhou, Z. Yan, L. Zhang and I. Bennion, *Opt. Express*, 2011, **19**, 11769–11779.
- 92 S. Ho, P. Herman and J. Aitchison, *Appl. Phys. A-Mater.*, 2012, **106**, 5–13.
- 93 S. Ho, M. Haque, P. R. Herman and J. S. Aitchison, *Opt. Lett.*, 2012, **37**, 1682–1684.
- 94 H. Y. Cheng, J. Grenier and P. R. Herman, *CLEO: 2013*, 2013, CM1H.3.
- 95 R. Taylor and C. Hnatovsky, *Opt. Express*, 2004, **12**, 916–928.
- 96 K. Sugioka, Y. Cheng and K. Midorikawa, *Journal of Physics: Conference Series*, 2007, **59**, 533.
- 97 A. Martinez, M. Dubov, I. Khrushchev and I. Bennion, *Electronics Letters*, 2004, **40**, 1170–1172(2).
- 98 N. Jovanovic, J. Thomas, R. J. Williams, M. J. Steel, G. D. Marshall, A. Fuerbach, S. Nolte, A. Tünnermann and M. J. Withford, *Opt. Express*, 2009, **17**, 6082–6095.
- 99 G. D. Marshall, R. J. Williams, N. Jovanovic, M. J. Steel and M. J. Withford, *Opt. Express*, 2010, **18**, 19844–19859.
- 100 C. Liao and D. Wang, *Photonic Sensors*, 2013, **3**, 97–101.
- 101 J. R. Grenier, L. A. Fernandes and P. R. Herman, *Opt. Express*, 2013, **21**, 4493–4502.
- 102 K. O. Hill and G. Meltz, *J. Lightwave Technol.*, 1997, **15**, 1263–1276.
- 103 L. Fernandes, M. Becker, O. Frazao, K. Schuster, J. Kobelke, M. Rothhardt, H. Bartelt, J. Santos and P. V. S. Marques, *IEEE Photonic Tech. L.*, 2012, **24**, 554–556.
- 104 D. Q. P. G. de Gennes, F. Brochard-Wyart, *Capillary and Wetting Phenomena: Drops, Bubbles, Pearls, Waves*, Springer, Ney York, 2004.
- 105 M. Zimmermann, P. Hunziker and E. Delamarche, *Microfluid. Nanofluid.*, 2008, **5**, 395–402.
- 106 H. J. Butt and M. Kappl, *Surface and Interfacial Forces*, Wiley-VCH, 2010.
- 107 S. Ho, *PhD thesis*, University of Toronto, 2013.
- 108 P. G. Kazansky, W. Yang, E. Bricchi, J. Bovatsek, A. Arai, Y. Shimotsuma, K. Miura and K. Hirao, *Appl. Phys. Lett.*, 2007, **90**, 151120.
- 109 M. Ohtsu, *J. Lightwave Technol.*, 1995, **13**, 1200–1221.
- 110 C. J. Tuck, R. Hague and C. Doyle, *Meas. Sci. Technol.*, 2006, **17**, 2206.
- 111 F. Toigo, A. Marvin, V. Celli and N. R. Hill, *Phys. Rev. B*, 1977, **15**, 5618–5626.
- 112 J. B. Taylor, A. L. Carrano and S. G. Kandlikar, *Int. J. Therm. Sci.*, 2006, **45**, 962 – 968.
- 113 H. Abu-Safia, R. Al-Tahtamouni, I. Abu-Aljarayesh and N. A. Yusuf, *Appl. Optics*, 1994, **33**, 3805–3811.